

RADIO-FREQUENCY SYNCHRONIZATION SYSTEM FOR FIBER-OPTIC QUANTUM NETWORKS

by

Stephen Chapman

A Thesis

Submitted to the Faculty of Purdue University

In Partial Fulfillment of the Requirements for the degree of

Master of Science in Electrical and Computer Engineering



School of Electrical and Computer Engineering

West Lafayette, Indiana

December 2023

**THE PURDUE UNIVERSITY GRADUATE SCHOOL
STATEMENT OF COMMITTEE APPROVAL**

Dr. Andrew M. Weiner, Chair

School of Electrical and Computer Engineering

Dr. Jason D. McKinney

School of Electrical and Computer Engineering

Dr. Joseph M. Lukens

School of Electrical and Computer Engineering

Dr. Sunil Bhave

School of Electrical and Computer Engineering

Approved by:

Dr. Dimitrious Peroulis

ACKNOWLEDGMENTS

I consider myself extremely lucky to have had the opportunity to conduct this research and write this thesis. It could not have happened without the support I received from everyone around me. First and foremost, I would like to thank my advisor, Professor Weiner, for being a great mentor and guiding me in this research every step of the way. I also greatly appreciate Professor McKinney for giving me valuable help and insight when I needed it most. Our collaborators at Oak Ridge National Laboratory, Dr. Joseph Lukens and Dr. Hsuan-Hao Lu, have also given me great direction on this project. All of these amazing people took time to help me on this journey, and I am eternally grateful.

My fellow labmates also gave me huge amounts of support and guidance. Dr. Nathan O'Malley and Suparna Seshadri worked with me on these projects day in and day out. I've asked my colleagues for help more times than I can count, and they've always been happy to help and patient with my endless questions.

I've also received boundless support from my family. My parents have always supported me personally and professionally. My girlfriend, Lauren, has also given me a tremendous amount of emotional support. I cannot express how blessed I feel to have these people in my life.

ABBREVIATIONS

BFC	Biphoton Frequency Comb
CW	Continuous Wave
DWDM	Dense Wavelength-Division Multiplexing
DSA	Digital Spectrum Analyzer
EOM	Electro-Optic Modulator
ESA	Electrical Spectrum Analyzer
FFT	Fast Fourier Transform
GVD	Group Velocity Dispersion
IM	Intensity Modulator
IMDD	Intensity Modulation and Direct Detection
JSI	Joint Spectral Intensity
ORNL	Oak Ridge National Laboratory
OSA	Optical Spectrum Analyzer
PD	Photo Detector
PM	Phase Modulator
PS	Pulse Shaper
QLAN	Quantum Local Area Network
RF	Radio Frequency
RFOF	Radio Frequency Over Fiber
QFP	Quantum Frequency Processor
QIP	Quantum Information Processing
SPDC	Spontaneous Parametric Down Conversion

TABLE OF CONTENTS

ABBREVIATIONS	4
LIST OF TABLES	7
LIST OF FIGURES	8
ABSTRACT	10
1 Introduction	11
1.1 Frequency Bin Entangled Qubits	11
1.2 Electro-Optical Modulation	13
1.2.1 Phase Modulation	13
1.2.2 Intensity Modulation	15
1.2.3 The Quantum Frequency Processor	16
1.3 Towards A Quantum Local Area Network (QLAN)	16
2 Identity Gate Experiments	18
2.1 Single Synthesizer Identity Gate	18
2.1.1 Setup	18
2.1.2 Results	19
2.2 Two Synthesizer Identity Gate with 10MHz Synchronization	20
2.2.1 Setup	20
2.2.2 Results	21
2.3 Identity Gate Simulation	23

2.4	Identity Gate with RF Over Fiber Synchronization	26
2.4.1	RF Over Fiber Setup	26
2.4.2	Identity Gate With RF Over Fiber	28
2.4.3	Identity Gate Over Long Distances	29
2.5	Conclusions	32
3	Nonlocal Modulation Cancellation	35
3.1	Background	35
3.2	Setup	36
3.3	Methods	37
3.4	Results	38
4	Conclusion and Future Work	41
	REFERENCES	42

LIST OF TABLES

2.1	Loss calculated by measuring power before and after spool. Therefore, these numbers also include the loss of the fiber optic connector used to connect the spool.	29
2.2	First two rows show 30 min drift of the first order sidebands. The last row is the amplitude of the first order sidebands at the beginning of the experiment, relative to the carrier.	32

LIST OF FIGURES

1.1 BFC generation (a) via SPDC using a nonlinear waveguide and a cavity filter and (b) via SFWM in a nonlinear ring resonator.[9]	12
1.2 An intensity modulator transmission diagram. A sinusoidal drive voltage yields sinusoidal optical modulation at the same frequency [14].	15
1.3 The WSS routes parts of the spectrum to nodes in the star configuration. Entanglement allows communication between any nodes as seen in the Full Mesh topology [18].	17
2.1 The spectra of each individual phase modulator before setting identity gate. First order sidebands are approximately equal in power to the main lobe. The two spectra look almost exactly the same, which is desired for the identity gate.	18
2.2 Setup diagram for the identity gate test with a single RF oscillator.	19
2.3 30 minute stability test results for the identity gate with a single oscillator driving both PMs.	20
2.4 Setups for two synthesizer identity gates. Top: Two synthesizers each connected to the 10 MHz clock. Bottom: Synthesizers connected to each other with one connected to the clock.	21
2.5 Two synthesizer stability test results. The left and right figures correspond to the top and bottom setups in Fig.2.4 , respectively.	22
2.6 Left: A screenshot of the DSA showing the two 19 GHz signals. Right: The time lag between the RF signals over the 5 minute stability test is plotted. .	23
2.7 Comparing simulation results to experimental data. The phase offset from ideal was varied. The experimental and simulated resulting change in first order sideband amplitude is plotted.	24
2.8 Correlation between time offset from ideal identity gate and first order sideband amplitude. The experimental data is the same as the previous figure. .	25
2.9 The identity gate setup where the second phase modulator is driven by an RF signal that has been sent over fiber using IMDD. PS1 is pulse shaper, discussed in Section 2.4.3.	26
2.10 Experimental photodetector output plotted against theoretical output power, which is proportional to the square of the Bessel function of the first degree.	27
2.11 Identity gate stability test with the RF over fiber system.	28
2.12 The pulse shaper's programmed discrete quadratic phase overlayed with an OSA trace. It is important that the phase discontinuities occur between the sidebands.	30

2.13 Four 30 minute stability tests with different spools. a) 200m, b) 700m, c) 1100m, d) 5500m. Only the 5500m spool test drifts enough to appear significant on these traces.	31
2.14 Identity gate with single oscillator. The phase is adjusted to mimic the sideband drift from the 5500m stability test at $t = 0$ and $t = 30$ minutes.	33
3.1 A diagram of the setup for nonlocal modulation cancellation.	37
3.2 JSI data with: a) No RF signal b) RF modulation cancelled by destructive interference c) RF modulation interfering constructively. The acquisition time was 2 seconds per bin. For a and b the CAR ≈ 25	39
3.3 The 5th row of Fig. 3.2 a and b plotted. Cancelled sidebands are similar in magnitude to the original, ideal values.	40
3.4 Left: Simulated sidebands for two PMs in series driven in phase. Right: The 5th row of Fig. 3.2 c , where the two PMs were driven in phase.	40

ABSTRACT

This thesis discusses the use of a fiber optic system to synchronize GHz frequency radio-frequency signals over distances of up to 5 km, and its future applications in quantum communications. The stability of the synchronization is assessed by an ‘identity gate’, where each radio-frequency signal drives a phase modulator, and the frequency profile of a continuous wave laser sent through both modulators indicates the stability of the RF signals relative to one another. Experimental results indicate that 19 GHz signals synchronized over 5.5 km drifted less than 1 ps over 30 minutes. This is superior to the radio-frequency synthesizers’ built in synchronization method and to other commonly used protocols. To illustrate an application, the system was employed in a quantum nonlocal modulation cancellation experiment. Joint spectral characterization of the biphotons shows that this synchronization scheme can be used for nodes in a quantum communications network. More specifically, possible future applications of this technology include use in a photonic quantum local area network at Oak Ridge National Laboratories.

1. Introduction

The phenomenon of entanglement has been a topic of great interest ever since its discovery in the early 20th century. Mathematically, a quantum state is entangled when its statevector cannot be factored into a tensor product of two (or more) states [1]. The nonclassical physical properties of entangled particles are what make them so intriguing. One such property is that measurements of entangled particles can be strongly correlated regardless of the distance separating the particles. In 1964 John Stewart Bell devised a way to test for ‘hidden variables’ in entanglement [2], and later experiments based on his theorem showed that the quantum correlations of entangled particles are truly nonlocal [3], [4]. This has lead to decades of research devoted to developing a practical method of quantum communication. The research presented in this thesis works toward a quantum communication network using the frequency of photons to encode information and fiber optic cables to distribute them.

1.1 Frequency Bin Entangled Qubits

The idea to use the frequency degree of freedom for quantum information technology started to gain traction when discretely encoded frequency entanglement was first demonstrated [5]. A pair of continuous frequency entangled photons can be created via spontaneous parametric down conversion (SPDC). The two-photon state can be theoretically written as

$$|\Psi\rangle = \int \Phi(\omega) |\omega_0 + \omega\rangle_S |\omega_0 - \omega\rangle_I d\omega \quad (1.1)$$

Where Φ is the line shape function. The total energy of the biphoton is conserved, but the energy (frequency) of each individual photon is in a superposition centered around ω_0 . [6] The discrete frequency bins are selected by sending the photons through narrowband filters or a Fabry-Perot cavity. Alternatively, frequency bin entangled photons can be generated through spontaneous four-wave mixing in a microring resonator. Both methods create several discrete and equidistant frequency bins. Hence, it is often referred to as a biphoton frequency comb (BFC) [7]. Additionally, every frequency bin can be utilized, giving the photon several levels for computation. The terminology for this is a “qudit”, where the “d”

refers to the $d > 2$ levels of computation [8].

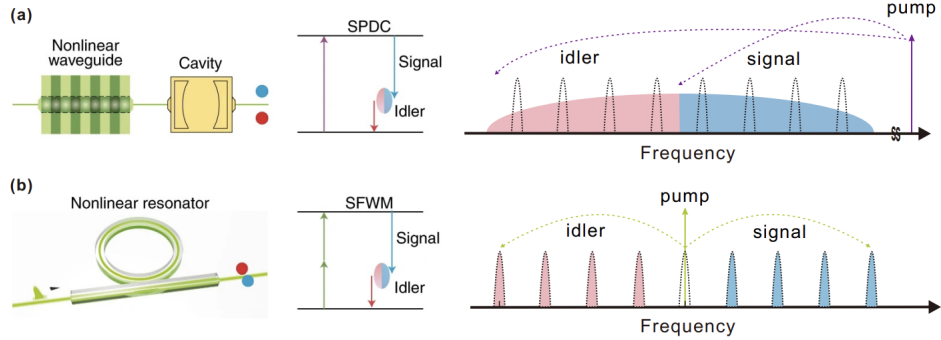


Figure 1.1. BFC generation (a) via SPDC using a nonlinear waveguide and a cavity filter and (b) via SFWM in a nonlinear ring resonator.[9]

Mathematically, the state of the BFC can be written as an extension of equation (1.1)

$$|\Psi_{BFC}\rangle = \sum_{k=1}^N \alpha_k |k_S, k_I\rangle = \sum_{k=1}^N \alpha_k \int \Phi(\omega) |\omega_0 + \omega\rangle_S |\omega_0 - \omega\rangle_I d\omega \quad (1.2)$$

Where $|k_S, k_I\rangle$ indicates the k th comb line pair and α_k is the joint amplitude and phase of the k th comb line pair [10].

High dimensionality and multipartite entanglement are two of many advantages to using frequency encoded photons for quantum information processing (QIP). Photons are the best way to transmit quantum information over long distances, and they also operate at room temperature. Quantum microcombs are also a very practical platform for generating the entangled states. Additionally, the pre-existing fiber optic telecommunication infrastructure can be utilized for quantum state transportation and manipulation. Together, all these benefits make frequency bin entangled photons a serious option for quantum communication and information systems [8].

SPDC is a relatively practical way to generate entangled photons. In this nonlinear optical process a pump photon of frequency ω_0 spontaneously becomes two photons whose frequency is centered around $\omega_0/2$. Since these two photons were created simultaneously and spawned from a pump photon with a well defined frequency, they have entanglement correlations

in both time and frequency [11]. Experiments in this thesis use pulse shapers (PSs) to carve out the frequency bins. Due to the entanglement, when the k th signal bin is selected and detected, correlations are measured in the k th idler bin, and no other frequency bin. Modulating the photons, as discussed below, changes these correlations and can be used for communication protocols.

1.2 Electro-Optical Modulation

All electro-optical modulation discussed in this thesis stems from the Pockels' effect. The Pockels' effect, also called the linear electro-optic effect, is when a material's dielectric tensor changes proportionally to the strength of an applied electric field. The term "linear" in the name refers to the linear relationship between the electric field strength and the change in the dielectric tensor [12]. The Pockels' effect is actually a $\chi^{(2)}$ nonlinear effect. Since it is an even-order nonlinear effect, it can only occur in non-centrosymmetric (i.e. without a center of inversion) crystals [13] such as LiNbO₃, which is the material used in the electro-optic modulators (EOMs) discussed here. This section focuses on phase modulators and intensity modulators driven by sinusoidal RF signals.

1.2.1 Phase Modulation

To obtain phase modulation, a sinusoidal drive voltage is applied to the lithium niobate.

$$V(t) = V_{RF} \sin(\omega_{RF} t) \quad (1.3)$$

Since the refractive index changes proportionally to this voltage and the optical path length is proportional to the refractive index, the optical field at the output of the phase modulator obtains a sinusoidal phase term [14]:

$$E_0(t) = \gamma e^{i(\omega t + \phi(t))} \quad (1.4)$$

where

$$\phi(t) = \phi_0 \sin(\omega_{RF}t) = \frac{\pi V_{RF}}{V_\pi} \sin(\omega_{RF}t) \quad (1.5)$$

where V_π is the voltage required to produce a π phase shift in the phase modulator. The amplitude of this oscillation is called the modulation index [15]. Using the Jacobi-Anger expansion [16] and equation (1.4), we obtain

$$\text{Re}\{E_0\} = \gamma \sum_{k=-\infty}^{\infty} J_k(\phi) \cos(\omega t + k\omega_{RF}t) \quad (1.6)$$

Where $J_k(\phi)$ is Bessel Function of the first kind. Also, $J_{-n} = e^{in\pi} J_n$. This opposite phase between sideband pairs is the reason that phase modulation cannot be seen via direct detection [10].

In the frequency domain, sidebands appear on both sides of the optical carrier. The first order sidebands have spacing from the carrier equal to the RF frequency. All integer harmonics sidebands will also appear. The amplitude of the nth order sideband pair is equal to the corresponding nth order Bessel function evaluated at the given modulation index, ϕ . One particular setup to note is when two phase modulators are placed in series, and the second PM is driven π radians out of phase with respect to the first PM but with the same modulation depth. In this case the sidebands created by the second PM will interfere destructively with those of the first PM. This causes all the sidebands to cancel, and the output will be the original carrier. Since the output is the same as the input, this is referred to as the 'identity gate'.

In the third chapter of this thesis, a signal-idler pair is phase modulated. In the quantum regime, the effect of phase modulation on the a signal idler pair in the k th mode is

$$\hat{m}_S |k\rangle = \sum_{n=-\infty}^{\infty} J_n(\phi) \left| k + \frac{n\omega_{RF}}{\Delta\omega} \right\rangle, \quad \hat{m}_I |k\rangle = \sum_{l=-\infty}^{\infty} J_l(\phi) \left| k + \frac{l\omega_{RF}}{\Delta\omega} \right\rangle \quad (1.7)$$

where $\Delta\omega$ is the free spectral range. As in the classical case, the modulation creates an infinite number of equally spaced sidebands. Now, in the quantum regime, the Bessel function

gives the probability amplitude of each sideband [10].

1.2.2 Intensity Modulation

Intensity modulators (IMs) are comprised of a Mach-Zehnder Interferometer in which both arms are an electro-optic material such as LiNbO₃. Voltages are applied to one or both of the arms, and intensity modulation results when the two signals interfere. A transfer function for an IM is depicted in Fig. 1.2. A DC bias voltage determines the baseline amount of optical transmission. The sinusoidal RF voltage oscillates the amount optical transmission about the baseline DC voltage level. The relevant application of IMs in this thesis is intensity modulation and direct detection (IMDD). In IMDD, the intensity modulator encodes information onto the light via the RF signal. When the light is detected, the RF signal can be retrieved. For this application the DC bias should be set in quadrature, meaning at a point where the transmitted optical power is the midpoint of the peak and null transmitted powers. Also, the modulation depth should be such that the modulator oscillates between peak transmission and null transmission [14].

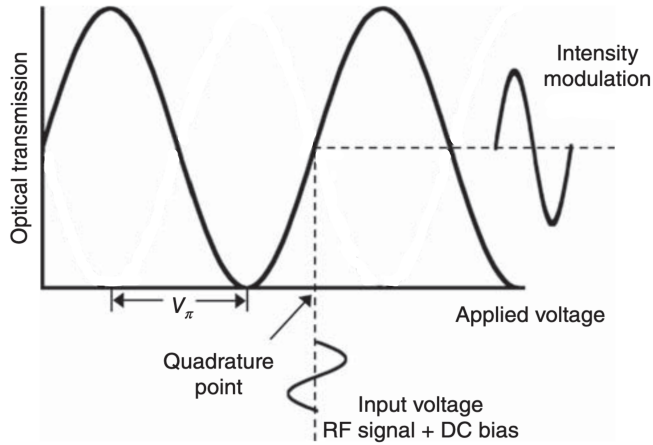


Figure 1.2. An intensity modulator transmission diagram. A sinusoidal drive voltage yields sinusoidal optical modulation at the same frequency [14].

A mathematical treatment for IMs can be done, and it is similar to the PM equations above. In fact, the optical power spectra of dual-sideband phase modulation and dual-sideband intensity modulation driven at the same modulation index are indistinguishable. The difference between the two modulation schemes lies in the phase of the sidebands. For phase modulation the sideband pairs are π out of phase, leading to no detectable RF frequencies. The phase of intensity modulation sidebands from a push pull modulator (where the voltage is split between both paths) allow the odd-order sidebands to produce an RF photocurrent under direct detection [14].

1.2.3 The Quantum Frequency Processor

If frequency bin entangled photons are to be used as qubits, a universal set of quantum gates is necessary for gate-based QIP. Divincenzo's criteria [17] states that with just single-qubit rotations and a two-qubit entangling gate, any arbitrary quantum operation is possible. As discussed above, EOMs can generate sidebands that can be used as frequency bins. But if only an EOM is used, the dimension of the Hilbert space will not be conserved. The QFP is constructed of a Fourier transform pulse shaper sandwiched between two EOMs. The pulse shaper can control the phase of each individual frequency bin. With the correct phase settings, all of the significant sidebands will remain in the desired Hilbert space after passing through the second EOM. This allows the dimensionality of the system to remain constant. Additionally, a sequence of alternating EOMs and PSs can create any unitary transformation on d frequency bins with $\mathcal{O}(d)$ components [9].

1.3 Towards A Quantum Local Area Network (QLAN)

Researchers at Oak Ridge National Laboratory (ORNL) have created a Quantum Local Area Network (QLAN) with nodes spatially distanced on the order of 1 km [18]. In their configuration, encoded photons are sent from the source through a wavelength selective switch (WSS) to each node. By using the nonlocal properties of entanglement, the nodes can com-

municate with each other in a full mesh. The system's topology is depicted in Fig. 1.3

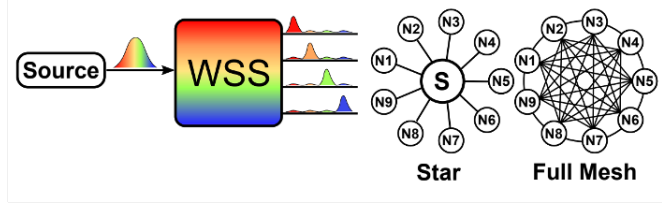


Figure 1.3. The WSS routes parts of the spectrum to nodes in the star configuration. Entanglement allows communication between any nodes as seen in the Full Mesh topology [18].

One of the next steps for the QLAN is to have a QFP at each node so frequency bin entangled qubits can be used as a method of communication between nodes. With a QFP at each node, frequency bin entangled qubits can be used as a method of communication between nodes. A technical challenge impeding this idea is that the high frequency RF signals driving the EOMs in the QFPs need to be synchronized across the spatially separated nodes to ensure high-fidelity quantum operations. The existing QLAN used GPS to synchronize the distant nodes in order to time coincidence windows of 10 ns [18]. However, the QFPs will be driven in the K-Band (18-27 GHz), where the period of the signal is \sim 50 ps, necessitating synchronization precision on the order of 1 ps.

The second chapter of this thesis documents progress towards this high precision timing synchronization scheme. Two phase modulators (PMs) are used to represent QFPs at two nodes. They are driven at 19 GHz. The two PMs are driven at the same modulation depth and π radians out of phase to create the identity gate explained above. Experimentally, it is possible to cancel the sidebands to almost -40 dBc. Once the identity gate is established, any amplitude or phase drift in the RF signals driving the PMs will cause an increase in sideband amplitude. This provides an accurate method to measure how well distant EOMs can be synchronized.

2. Identity Gate Experiments

2.1 Single Synthesizer Identity Gate

2.1.1 Setup

In this experiment a 10 mW Agilent 81940a tunable CW laser at 1560.61nm is sent through two PMs to an optical spectrum analyzer. An Agilent E8257D RF synthesizer is set to 19 GHz and 23.50 dBm. The 19 GHz signal is split 50/50. After the splitter, one end goes through a variable attenuator and then to PM1. The other end goes through a variable phase shifter and then to PM2. The variable attenuator is used to match the modulation depths of the PMs, and the phase shifter is used to achieve the π phase shift between PMs.

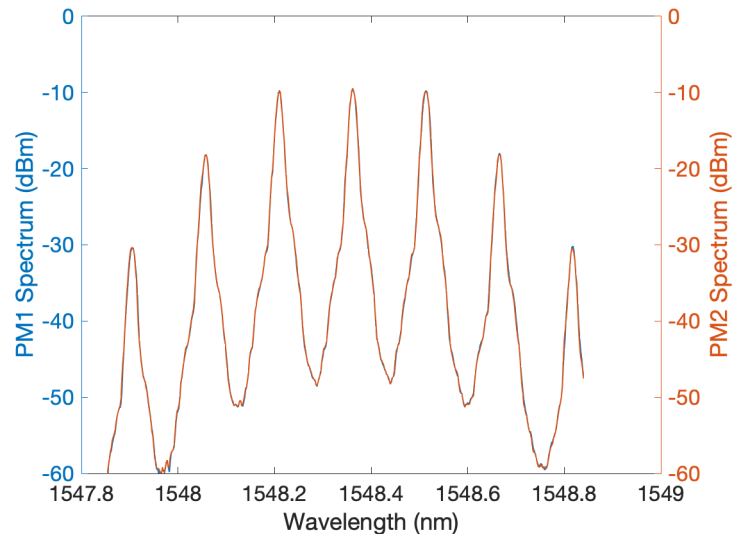


Figure 2.1. The spectra of each individual phase modulator before setting identity gate. First order sidebands are approximately equal in power to the main lobe. The two spectra look almost exactly the same, which is desired for the identity gate.

PM1 and PM2 have V_π specifications of 4.4V and 4.6V at 19 GHz. Therefore, to equate the modulation depths, they must be driven with different RF powers. To standardize experiments, in all identity gate experiments the PMs were driven with an RF power such that the first order sidebands were equal in magnitude to the main lobe (see Fig. 2.1).

This corresponds to a modulation index of approximately 1.42 radians. Additionally, this modulation index was used because it is desirable for future applications in the QLAN.

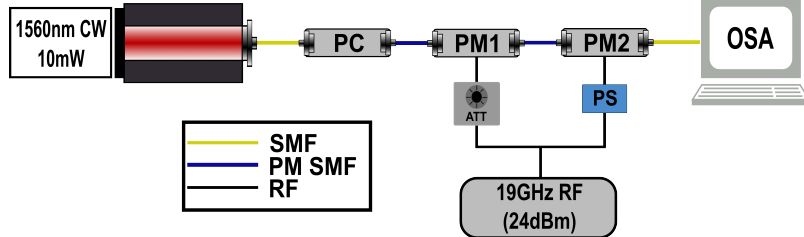


Figure 2.2. Setup diagram for the identity gate test with a single RF oscillator.

When initializing the identity gate, the output spectrum of each individual PM is measured to ensure the modulation depth is ≈ 1.42 , as discussed above. Next, the spectrum of the PMs in series (the setup in Fig. 2.2) is observed on the OSA. To obtain an identity gate, the variable attenuator and phase shifter are adjusted until the spectrum's sidebands are minimized.

For this identity gate experiment, and those discussed below, the sidebands are cancelled as much as possible and then the setup is left untouched and OSA traces are taken over a period of time to assess the stability of the system.

2.1.2 Results

A 30 minute stability test was performed. As can be seen in Fig. 2.3, the initial sideband extinction is -48.08 dBc. Over the 30 minute duration, the right sideband drifts 1.77 dB and the left sideband drifts 1.49 dB.

A multitude of factors could be responsible for this sideband drift including phase shifter and attenuator drift, polarization drift, or OSA uncertainty. All of these effects should be negligible, and, as expected, the 1.77 dB sideband drift is negligibly small. As will be discussed in Section 2.3, the magnitude of sideband drift is not enough to characterize stability

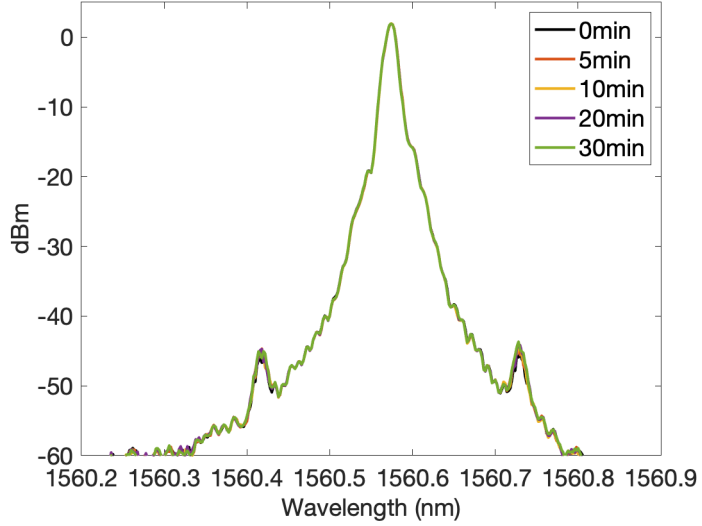


Figure 2.3. 30 minute stability test results for the identity gate with a single oscillator driving both PMs.

on its own. The lower the sidebands are relative to the carrier (dBc), the more sensitive they are to timing drift. This can be seen in [Fig. 2.8](#). The results discussed in Section 2.3 estimate that the single oscillator identity gate's 1.77 dB drift at approximately -48 dBc corresponds to less than a tenth of a ps timing drift. The uncertainty of this method for converting sideband drift to ps drift has not yet been evaluated, so the result should be treated as a simple estimate. Nonetheless, this single oscillator result shows stability and ample sideband cancellation in the ideal case.

2.2 Two Synthesizer Identity Gate with 10MHz Synchronization

2.2.1 Setup

The Agilent E8257D synthesizers have input/output ports for a 10 MHz synchronization signal. Experiments in this section test whether an identity gate can be constructed using two Agilent synthesizers, with each synthesizer driving one PM. The clock signal used for these experiments is an EndRun Technologies GPS Disciplined Oscillator. In the first inves-

tigation, the two synthesizers are synchronized to the common 10 MHz clock signal. In the second investigation, one synthesizer is synchronized to the 10 MHz clock, and the second synthesizer is synchronized to the first synthesizer. These two synchronization setups are depicted in **Fig. 2.4**.

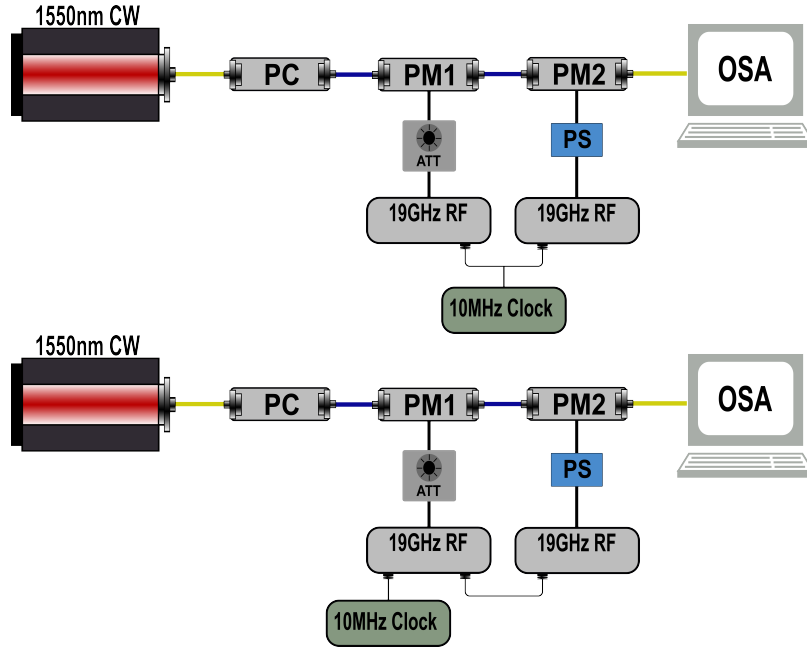


Figure 2.4. Setups for two synthesizer identity gates. **Top:** Two synthesizers each connected to the 10 MHz clock. **Bottom:** Synthesizers connected to each other with one connected to the clock.

2.2.2 Results

In both setups, sideband cancellation was obtained. In the first (top) setup, the first order sidebands were reduced to -32.3 dBc. The second (bottom) setup had notably better sideband cancellation of -42.9 dBc. We are not sure why the second setup yielded better initial sideband cancellation.

Stability data was taken, but only 5 minute stability tests were performed because after only 5 minutes it was clear that these setups were not stable. During the 5 minutes, the first

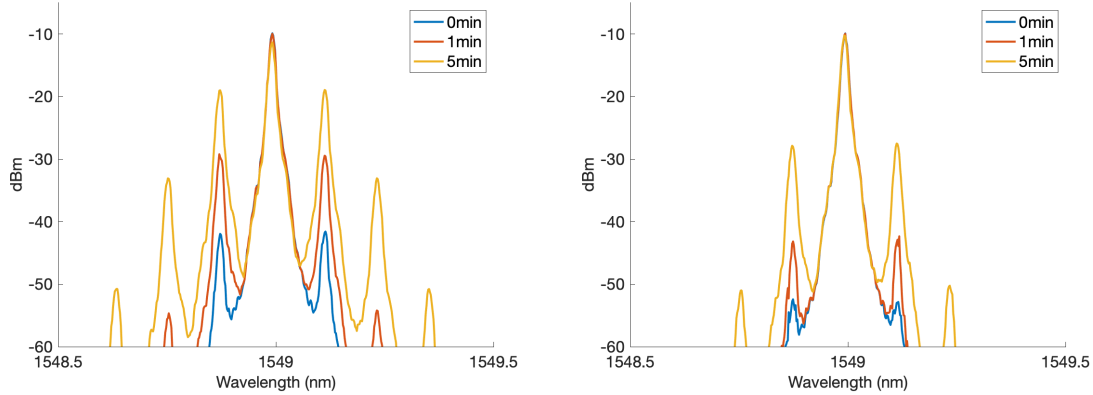


Figure 2.5. Two synthesizer stability test results. The left and right figures correspond to the top and bottom setups in [Fig. 2.4](#), respectively.

order sidebands of setup 1 and setup 2 drifted 24.6 dB and 25.1 dB, respectively.

The drift seen in this setup was much more than anticipated. To analyze it further, a 30 GHz Agilent Technologies Digital Signal Analyzer (DSA) was used. The RF cables were disconnected from the PM inputs and connected to two channels on the DSA. This allowed us to view the two 19 GHz signals directly in the time domain. With the two oscillators connected as shown in the bottom setup of [Fig. 2.4](#), DSA traces were taken every minute for 5 minutes. These traces show the relative phase offset between the RF signals. An examination of these traces (plotted in [Fig. 2.6](#)) shows that the RF signals drifted approximately 3 ps relative to each other over the 5 minute test.

This DSA data confirms that the RF signals are drifting on the ps scale relative to one another over the course of just a few minutes. The error bars in the plot in [Fig. 2.6](#) come from uncertainty in the DSA readings. The DSA is set to trigger at the 0 mV level of channel 4 (red). Channel 1 (yellow) then has a width of approximately 1 ps. Therefore, error bars of ± 0.5 ps were applied.

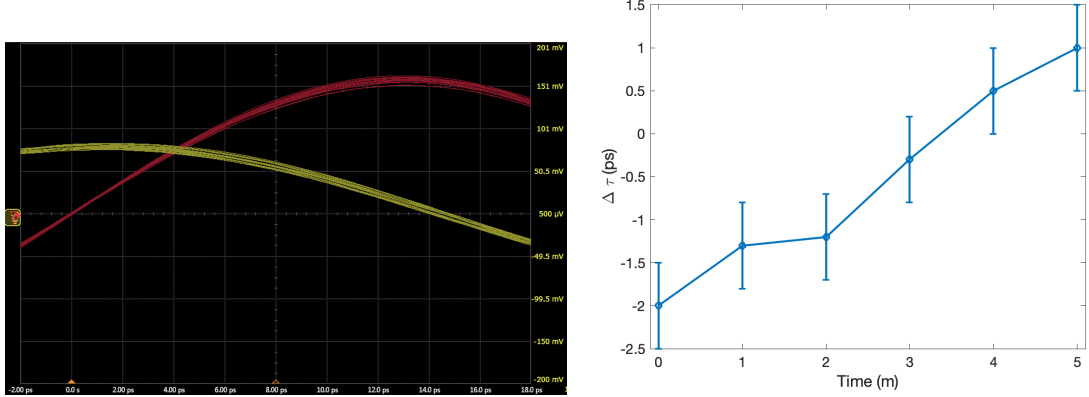


Figure 2.6. Left: A screenshot of the DSA showing the two 19 GHz signals. **Right:** The time lag between the RF signals over the 5 minute stability test is plotted.

2.3 Identity Gate Simulation

A simulation modelling the two phase modulators in series was coded in Matlab. This simulation was useful to check that experiments were consistent with mathematical models. After verifying the accuracy of the simulation, it was eventually used to produce RF phase drift estimates from identity gate OSA data.

The simulation models the CW carrier laser as a delta function in the frequency domain. It then takes the FFT and applies the modulation described in Section 1.2.1 to compute the field after phase modulation.

$$E_{out}(t) = E_{in}(t)e^{iM \sin(2\pi f_m t)} \quad (2.1)$$

Where M is the modulation depth and f_m is the modulation frequency. The code then repeats this with an added π phase offset in the sin term to simulate the second PM. The user can choose to add a phase offset to the second PM to simulate non-ideal identity gates. The IFFT is then taken and the output spectrum is plotted, allowing the user to view the sideband amplitude corresponding to the input phase offset.

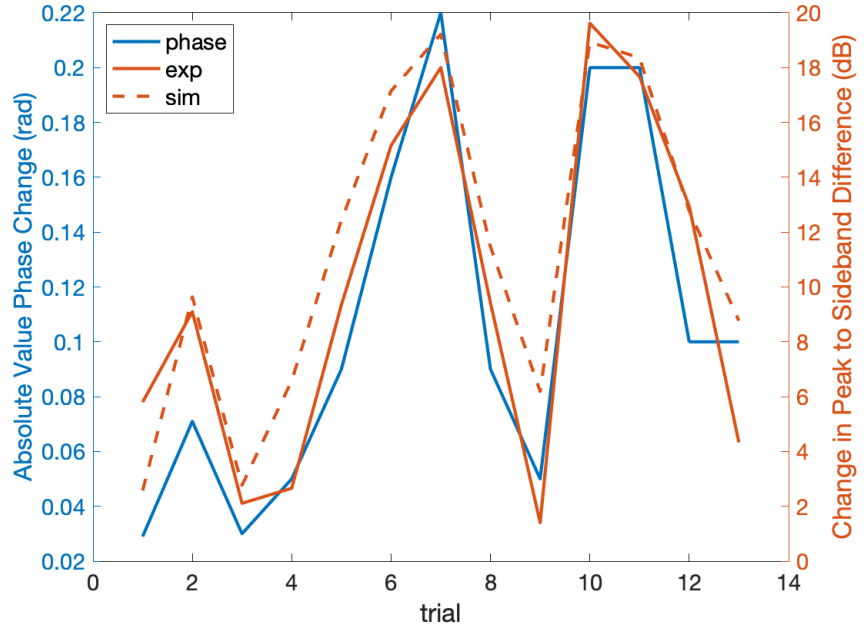


Figure 2.7. Comparing simulation results to experimental data. The phase offset from ideal was varied. The experimental and simulated resulting change in first order sideband amplitude is plotted.

The simulation's accuracy was assessed through agreement with experiment. The bottom setup in **Fig. 2.4** was used, except the RF phase shifter was removed. Instead, the second Agilent's internal phase offset abilities were used. The reason for this, and the reason why the two-oscillator setup was used, is because the oscillator's internal phase offset can set the phase to a thousandth of a radian. Whereas with the usual RF phase shifter, no quantitative information about the phase shift is available. Using this quantitative phase adjustment, the optimum identity gate was obtained. An OSA trace was taken and the phase, ϕ_0 , was noted. Then the phase was adjusted by a small amount to some ϕ_2 . Another OSA trace was taken and this second phase offset was noted. This process was repeated 13 times. Optimal identity gate was reset after each trial, and each trial was performed as quickly as possible (< 10 seconds) so that drift between the two oscillators would be negligible. The data gives a relation between the phase offset from optimum $\Delta\phi = |\phi_2 - \phi_0|$, and the resulting change in sideband amplitude. The phase offset, $\Delta\phi$, was then used as

inputs to the simulation, which then predicted an identity gate with sideband amplitudes. The phase offsets, experimental and simulated sideband amplitudes are plotted in [Fig. 2.7](#). The average discrepancy between experimental and simulated sidebands is 2.1 dB.

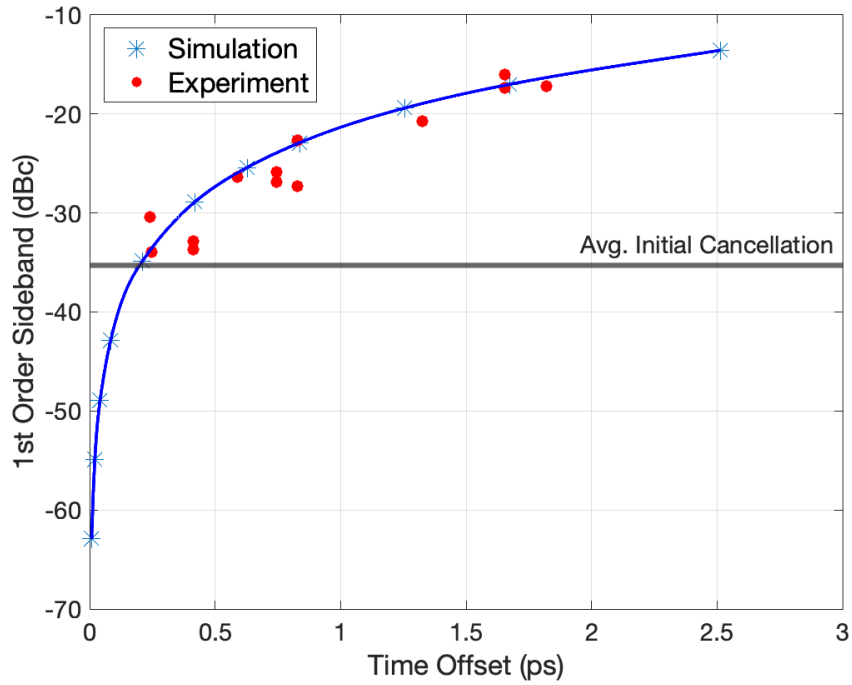


Figure 2.8. Correlation between time offset from ideal identity gate and first order sideband amplitude. The experimental data is the same as the previous figure.

Another way of visualizing the simulation's agreement with experiment is depicted in [Fig. 2.8](#). The red markers in this plot represent the same experimental data from [Fig. 2.7](#). The y-axis is now the dBc of the first order sideband plotted as a function of the time offset (derived from the phase offset). The blue markers are where a time offset has been entered into the simulation, and the output's sideband's dBc has been plotted. Not only does this another way to view the agreement between simulation and experiment, but it also provides a method for converting from experimental sideband drift to ps timing drift.

2.4 Identity Gate with RF Over Fiber Synchronization

2.4.1 RF Over Fiber Setup

The results in the previous sections showed that two-oscillator schemes were significantly less stable than a one oscillator identity gate. Therefore, we instead attempt to use one oscillator, and try to transport its signal to a distant PM. One procedure that has been used to transport RF signals over long distances is with an RF over fiber (RFOF) scheme. For this experiment intensity modulation and direct detection (IMDD), one of the simplest RFOF methods, is used. In the IMDD protocol, the synthesizer's RF signal drives an IM, which modulates a CW laser. The light that has been modulated by the IM can then be sent over long distances of fiber and eventually detected by a fast photodetector. The photodetector recovers the RF signal. Which, in this case, can be used to drive the second PM.

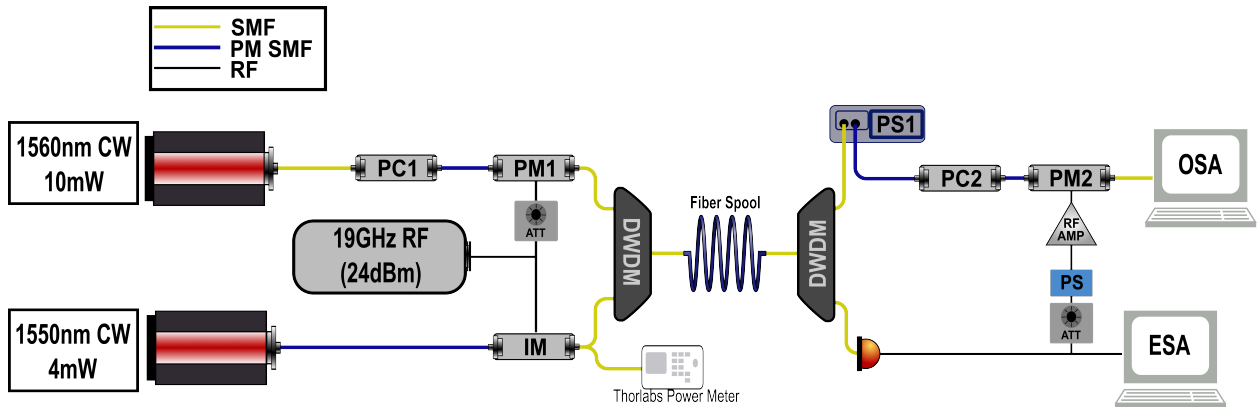


Figure 2.9. The identity gate setup where the second phase modulator is driven by an RF signal that has been sent over fiber using IMDD. PS1 is pulse shaper, discussed in Section 2.4.3.

Correctly setting up the RFOF system necessitated some characterization. The main active components for RFOF are the IM and fast photodetector (PD). The PD is an Optilab 23 GHz Balanced Photo Receiver, and the IM is a 20 GHz EOSpace IM with a DC $V_\pi = 2.4V$. In IMDD, the IM must be biased in quadrature. This was done by sending the balanced photodetector's second output to an electronic signal analyzer (ESA). First, the IM's optimum RF drive power was found by incrementally varying the RF power, and at

each incremental step the bias voltage was adjusted to maximize the photodetector's output power. As can be seen in **Fig. 2.10**, the optimal RF drive power is approximately 19 dBm. The theoretical result shown in the same figure shows that ideally the photodetector's output should be given by [14]

$$P_\Omega \propto J_1^2(\phi_{rf}) \quad (2.2)$$

Where ϕ_{rf} is the modulation depth and J_1 is the Bessel function of the first kind.

The IM was then driven at 19 dBm and bias was adjusted once again to maximize the photodetector's output power. Due to thermal fluctuations the optimal bias voltage would drift over time. The ESA was not accurate enough to measure this , but the drift was large enough of an effect to degrade the identity gate results. To solve this issue, the IM's output was split and a Thorlabs optical powermeter with a sensitivity of $1\mu W$ was attached to monitor the IM output. The bias voltage was manually controlled to keep the IM power output constant to within $\pm 5 \mu W$ during stability tests.

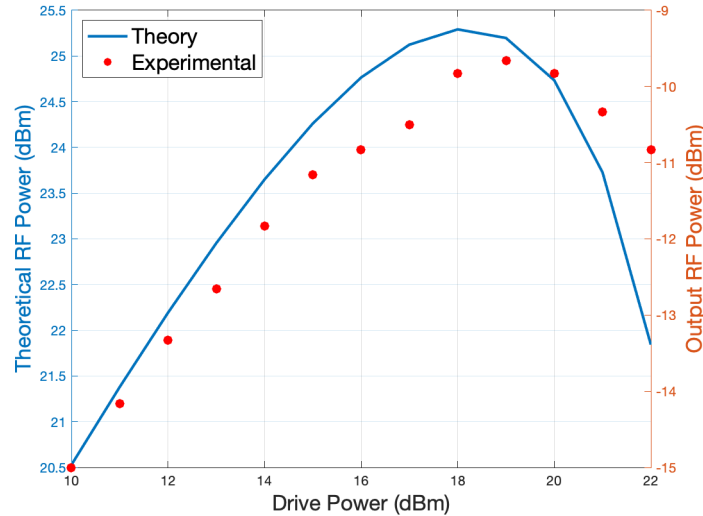


Figure 2.10. Experimental photodetector output plotted against theoretical output power, which is proportional to the square of the Bessel function of the first degree.

2.4.2 Identity Gate With RF Over Fiber

The RFOF system was incorporated into the identity gate setup as shown in [Fig 2.9](#). The identity gate setup involved the steps described in Section 2.1.2, with the addition of setting the IM bias for the RFOF section. Sideband cancellation was achieved, and a 30 minute stability test was performed. As can be seen in [Fig. 2.14](#), this setup yielded a stable identity gate with the left and right first order sidebands at -36.68dBc drifting 0.99 dB and 2.74 dB, respectively. Comparing this result with the results from Section 2.1.3 and Section 2.2.2, the RFOF setup has produced stability vastly superior to the 10MHz synchronization methods. And the RFOF's stability is close to the optimal stability of one oscillator.

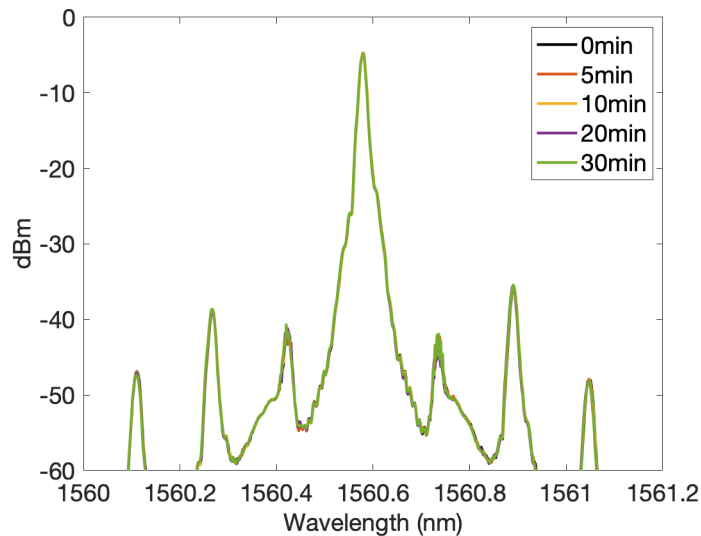


Figure 2.11. Identity gate stability test with the RF over fiber system.

It can be seen in [Fig. 2.14](#) that the 2nd and 3rd order sidebands are not as suppressed as the first order sidebands. This occurred only in the RFOF identity gate setups. After much investigation, the cause of this phenomenon was never completely determined. The higher order sidebands drift is negligible during stability tests, and they are well enough suppressed for QFP applications. For these reasons it was decided to ignore them.

2.4.3 Identity Gate Over Long Distances

With the successful stability test of the RFOF identity gate, the next step was to start putting distance between the two PMs. For nonlocal modulation cancellation applications approximately 100 m between the PMs is desired. For QLAN applications approximately 1-2 km between the PMs is desired. Fiber spools of: 200 m, 700 m, 1100 m, 5500 m were selected to test the capability of the system between long distances.

The loss of each fiber spool was measured and is displayed in **Table 2.1**. The 700 m and 1100 m spools are Corning SMF28E+. The 5500 m spool is Corning SMF-28(TM), and the 200m spool is Corning 9/125 SM.

	200m	700m	1100m	5500m
Measured Loss (dB)	0.3	0.7	0.6	1.1

Table 2.1. Loss calculated by measuring power before and after spool. Therefore, these numbers also include the loss of the fiber optic connector used to connect the spool.

The selected fiber spool was inserted between the DWDMs. This allowed the phase modulated signal and the intensity modulated signal to travel in the same fiber through the long distance of the fiber spool, and then be demultiplexed afterwards. This approach seemed to reduce thermal and other environmental effects.

These long distance tests required chromatic dispersion compensation. Chromatic dispersion, or group velocity dispersion (GVD) arises from the medium's refractive index causing the group velocity to depend on frequency. Nonzero GVD in this experiment means the frequency sidebands created by PM1 will have slightly different phases after propagating through the fiber spool. It becomes impossible to cancel all the sidebands, or even both first-order ones, because of the dispersion induced phase difference.

GVD manifests as a quadratic phase as a function of frequency. Mathematically

$$E_{out}(\omega) = E_{in}(\omega)e^{-i\frac{L}{2}\beta_2(\omega-\omega_0)^2} \quad (2.3)$$

And it can be derived [19] that any given wavelength λ offset by $\Delta\lambda = \lambda - \lambda_0$ arrives with a time delay given by

$$\Delta\tau(\lambda) = \frac{-2\pi c\beta_2\Delta\lambda L}{\lambda^2} \quad (2.4)$$

Using this equation with $\beta_2 = -26 \frac{fs^2}{mm}$ and the 1.1 km fiber spool, the time delay between the left and right first order sidebands is approximately 6 ps, which is about 0.7 radians of phase. This makes it impossible to cancel both first order sidebands at the same time, necessitating dispersion compensation.

The pulse shaper, a Finisar WaveShaper 1000s, is used to compensate for the chromatic

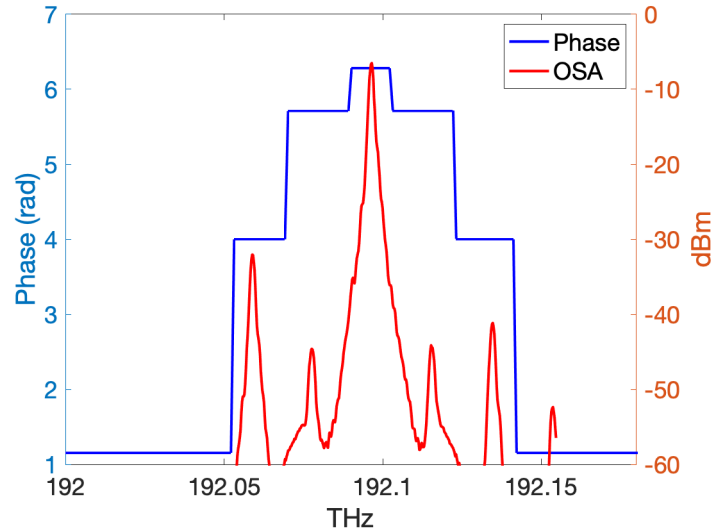


Figure 2.12. The pulse shaper's programmed discrete quadratic phase overlaid with an OSA trace. It is important that the phase discontinuities occur between the sidebands.

dispersion. A Matlab script was written to program it to apply a quadratic phase on the spectrum. Through mathematical estimation, along with trial and revision, the pulse shaper can set a quadratic phase equal and opposite in magnitude to the fiber's dispersion. The pulse shaper has a specification of 10 GHz resolution, and a phase discontinuity at one of the sidebands leads to undesirable results. Therefore, the quadratic is modelled discretely, with discontinuities between the sidebands. This can be seen in **Fig. 2.12**.

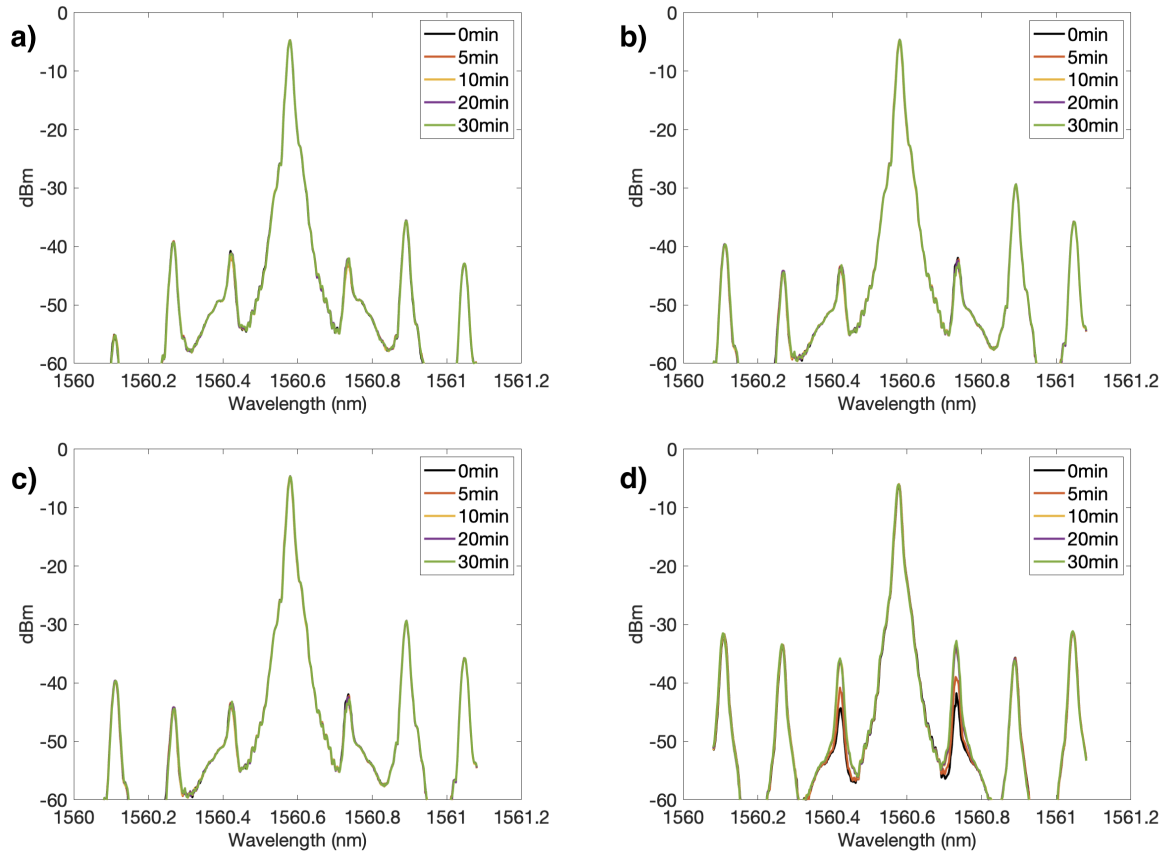


Figure 2.13. Four 30 minute stability tests with different spools. **a)** 200m, **b)** 700m, **c)** 1100m, **d)** 5500m. Only the 5500m spool test drifts enough to appear significant on these traces.

30 minute stability tests were performed with each fiber spool. The results are shown in the **Fig. 2.13**. For each figure, sideband analysis was performed. **Table 2.2** shows the numerical results of how much the first order sidebands drifted over the 30 minutes. The numbers for the initial sideband suppression in dBc were taken from whichever first order sideband was less cancelled.

	No Spool	200m	700m	1100m	5500m
Left Sideband (dB)	0.99	0.73	1.11	0.34	8.51
Right Sideband (dB)	2.74	0.93	2.61	0.86	8.97
Starting dBc	-38.15	-37.95	-39.19	-38.71	-38.31

Table 2.2. First two rows show 30 min drift of the first order sidebands. The last row is the amplitude of the first order sidebands at the beginning of the experiment, relative to the carrier.

This data shows that the RFOF identity gate setup is very stable with the 1100 m spool. The 700 m spool repeatedly performed worse than the 1100 m spool. This is likely because the 700 m spool's transmission is more susceptible to vary based on the fiber's orientation.

2.5 Conclusions

The stability tests discussed above show that the RFOF setup is able to maintain its original stability to distances of over 1 km. There is a large jump in distance from the 1100m spool to the 5500 m spool, and the decrease in stability is obvious. The >8 dB drift with the 5500 m spool looks very large compared to the shorter lengths. The important metric is the timing drift between RF signals. Using the simulation discussed in Section 2.3, the ≈ 9 dB drift starting at -38.3 dBc corresponds to approximately 0.5 ps of timing drift.

A 0.5 ps timing drift is an impressive number, so to corroborate this number a test was performed to convert sideband drift to timing drift using the DSA. The single oscillator identity gate from Section 2.1 was set up, and 20 dB taps were inserted at the RF inputs to PM1 and PM2. The taps' outputs were sent to channel 1 and channel 4 of the DSA. First,

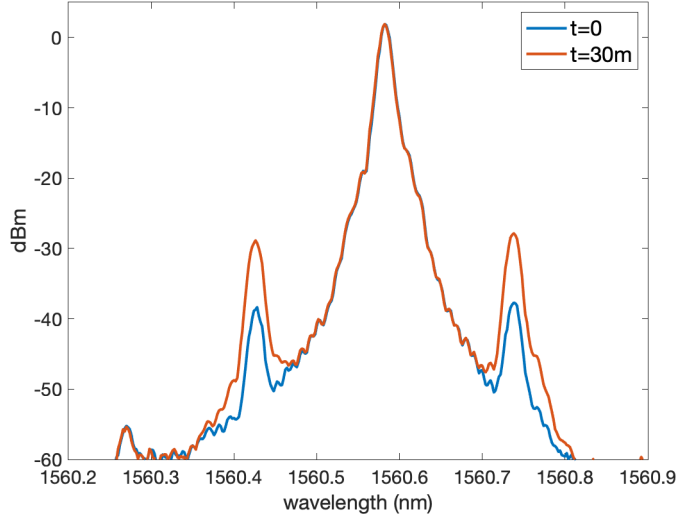


Figure 2.14. Identity gate with single oscillator. The phase is adjusted to mimic the sideband drift from the 5500m stability test at $t = 0$ and $t = 30$ minutes.

the phase shifter and attenuator were adjusted to obtain the best possible identity gate. Next, the phase shifter was adjusted, rising the first order sidebands to -39.9 dBc. OSA and DSA traces were taken. Then the phase shifter was adjusted again until the first order sidebands were at -30.26 dBc. OSA and DSA traces were taken again. This was an attempt to mimic the 5500 m identity gates at $t = 0$ and $t = 30$ minutes. Both settings were within 2 dB. The phase shift between these two identity gates can then be seen on the DSA, which showed a timing drift of 0.5 ± 0.5 ps. This agrees with the simulation result. Even with the DSA's relatively large uncertainty, the timing change is less than 1 ps.

Estimating timing drift numbers for the shorter spools is more complicated. The DSA experiment discussed in the previous paragraph cannot be applied here because the DSA is not accurate enough to give meaningful estimates. The timing drift could be assessed using the simulation, as the single oscillator identity gate was, but the simulation hasn't been experimentally verified at these levels. Additionally, for drifts of ≤ 1 dB at such low powers, other effects, such as the OSA's accuracy, come into question. For these reasons, the most responsible conclusion is to estimate the 5500m test's drift at ~ 0.5 ps and the drift in the

other tests is significantly less. Although there are not well defined numbers for timing drift, they are all satisfactory for use in synchronizing nodes in a QLAN at ORNL.

3. Nonlocal Modulation Cancellation

3.1 Background

The previous chapter detailed a method for synchronizing 19 GHz RF signals over long distances. The preliminary results of those classical experiments showcased timing drift of only a few hundred femtoseconds over 30 minute tests. This accomplishment is a vital preliminary step toward the deployment of QFP technology [9] in a QLAN, making quantum communication protocols including teleportation and entanglement swapping possible through frequency-encoded qubits and qudits [9][20]. In this chapter, the RF synchronization system is used once again, but this time it is tested in the quantum regime. This is done by performing a “truly” nonlocal modulation cancellation experiment on a pair of frequency-bin entangled photons.

Nonlocal modulation cancellation was initially proposed and implemented by Harris *et. al.* [21], [22]. In this experiment, a pair of frequency-entangled photons is split and each photon is directed to a PM. Due to the time-frequency correlations, sinusoidal phase modulation on one photon affects the other photon in the same manner. So the modulation of the idler photon can be either increased or nullified by the modulation of the signal photon depending on the relative phases of the two PMs. Not only is this experiment an interesting Fourier analogue to fiber optic dispersion cancellation [23]–[26] but is also a first step to more intricate entangled frequency qubit operations for communication [20].

The original nonlocal modulation cancellation experiment had the two PMs driven by the same RF oscillator in the same lab [22], making it not completely ‘nonlocal’. To our knowledge, every frequency-bin quantum information processing experiment that employs PMs synchronized with GHz frequencies has driven the two PMs with the split output of a single RF oscillator [27]–[31]. This is the simplest way to obtain phase stability over short distances, but the RF cable loss (typically several dB per meter) makes this unsuitable for real-world applications over network distances. Existing solutions for long distance time and frequency transfer either have too much jitter for 10 GHz synchronization—like White Rabbit [32], [33]—or they are extremely complex, with various combinations of bidirectional path-length stabilization and frequency combs [34], [35]. The approach discussed in this

thesis is relatively simple to setup, but is also stable enough to be used for distributed quantum frequency operations. And as a proof-of-principle demonstration, we conduct the first truly nonlocal modulation cancellation experiment on entangled photons.

3.2 Setup

The setup begins with a 778.5 nm CW laser (Toptica DL Pro) pumping a periodically poled lithium niobate (PPLN) waveguide heated to 37° C to maximize SPDC. The SPDC process emits pairs of entangled photons whose wavelength is centered at twice the pump wavelength, i.e. 1557 nm. The signal and idler photons are routed to different paths using pulse shaper PS1 (WaveShaper 4000A, Coherent Corp.). The signal photon goes to a polarization controller and then a phase modulator (PM1). The idler photon goes through the RFOF system discussed in Section 2.4. For the experiments in this chapter, the RFOF system carries the idler through the 200 m fiber spool. This length was chosen because it is a significant distance, but also short enough to prevent GVD and Raman scattering from significantly hindering the results. Nonetheless, to obtain optimal results GVD compensation was still implemented using PS2 and the same method discussed in Section 2.4.3. It should also be noted that the DWDMs used in the RFOF system here are Opneti High Isolation DWDMs, which have > 40 dB isolation. And two of these DWDMs were cascaded at the multiplexing site to stop crosstalk from the 4 mW RFOF laser leaking into the idler channel. After demultiplexing, the idler photon goes through a polarization controller and then a phase modulator (PM2). As in previous experiments, the PMs are driven at $\omega_{RF}/2\pi = 19$ GHz and modulation depth $\delta = 1.42$ radians. After each PM is a pulse shaper (PS2 or PS3, each a WaveShaper 1000S from Coherent Corp.) in signal and idler paths, respectively, and the output of these pulse shapers are routed to superconducting nanowire single-photon detectors (SNSPDs, Quantum Opus). The detector outputs are sent to an event timer (Swabian Time Tagger Ultra).

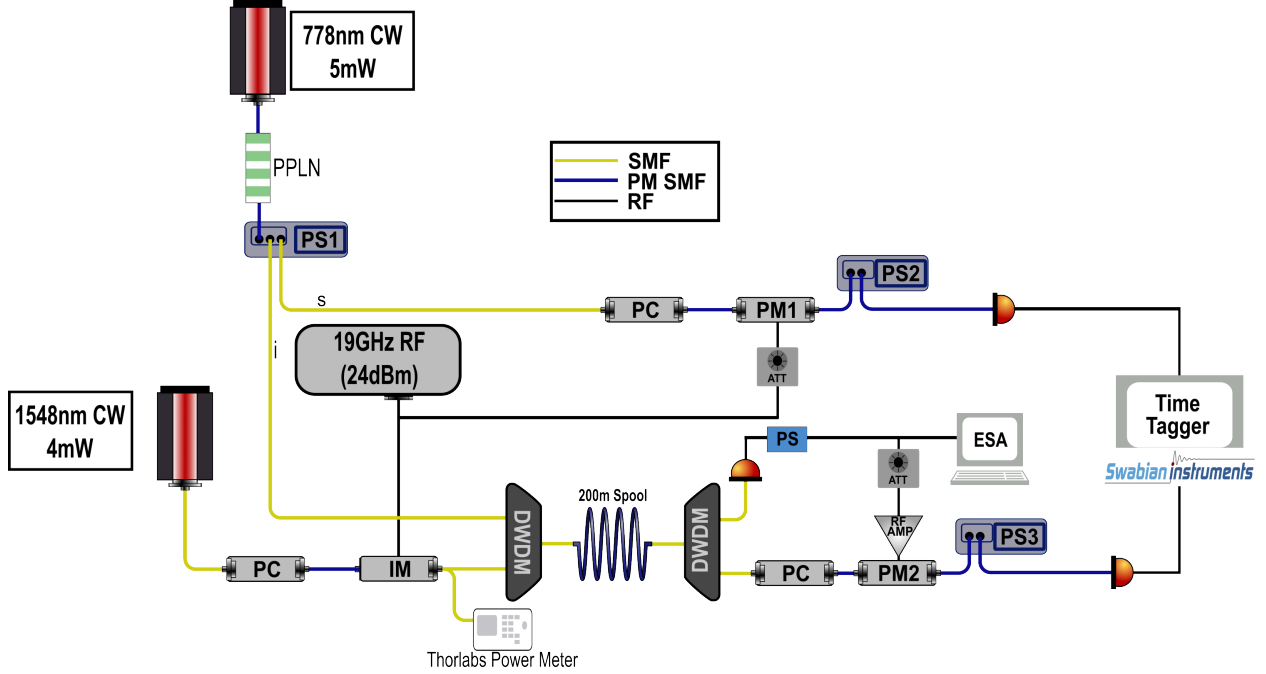


Figure 3.1. A diagram of the setup for nonlocal modulation cancellation.

3.3 Methods

Before sending in any quantum light, a classical laser is sent through the PMs in series to an OSA. This classical identity gate is used to ensure the PMs are driven at the same modulation index. Then the setup is restored to as shown in [Fig. 3.1](#). PS2 and PS3 are set to fully open and the RF signal is turned off. Using PS1, a 140 GHz-wide frequency band was opened at 1550.9 nm on the signal spectrum and at the center of the DWDM passband. PS1 selects the corresponding 140 GHz-wide frequency band in the idler spectrum and routes it to the other path. The polarization controllers in the setup are then tuned to maximize measured coincidence counts. 12 GHz-wide frequency bins are selected using PS2 and PS3, and the bins are scanned to obtain a joint spectral intensity (JSI) measurement of the signal and idler over the frequency band selected by PS1. Since the RF modulation frequency of 19 GHz creates sidebands every 1 GHz, each index in the JSI is separated by 19 GHz so that the modulation sidebands can be properly viewed. It was attempted to set the relative RF phase between the signal and idler PMs by encoding a linear spectral phase onto the signal

frequency band in PS1. This linear phase on the photon would manifest a time delay, which is identical to shifting the RF phase on that photon [29]. However, the resolution of the pulse shaper was not adequate enough for this method. When tried, interference between pulse shaper pixels changed the amplitudes of some photons, causing unwanted features in the JSIs. Instead, the phase for modulation cancellation was found by using the RF phase shifter and maximizing coincidence counts on the anti-diagonal of the JSI.

3.4 Results

First, a JSI was taken with the RF signal turned off. This is to show signal-idler frequency correlations in the ideal case. Next, the RF signal was turned on and the RF phase was adjusted to achieve optimum modulation cancellation. In the next trial the RF phase was shifted to set the modulators in phase. When modulators of this modulation index are in phase, the second order sidebands are maximized. This means that bins 5,7 and 7,5 on the JSI will be maximized. This knowledge was used to set the phase for the in phase modulation trial.

It is evident that the JSI with modulation cancellation is very similar to the JSI with RF off. There are discrepancies at signal-idler indices 2,2 and 8,8. These are present because the modulation of these edge bins creates sidebands that are outside the DWDM passband. They get attenuated and therefore cannot be brought back into the Hilbert space to contribute to their original bins.

Examining a single line or column in a JSI is equivalent to fixing the frequency bin of one of the biphotons and scanning frequency bin of the other biphoton. Plotting this, we get a picture analogous to OSA traces of two PMs in series. **Fig. 3.3** plots the fifth row of JSIs from **Fig. 3.2** without modulation and with modulation cancellation enabled. We observe that the correlations in the bin pairs with modulation cancellation enabled agree well with that of the original spectrum with modulation turned off. To evaluate the in phase modulation JSI, it is compared to the simulation result. Below shows a normalized plot of the fifth row of **Fig. 3.2c**. The simulation discussed in Chapter 2 was used to predict the relative amplitudes of the sidebands when two modulators are driven in phase with modulation

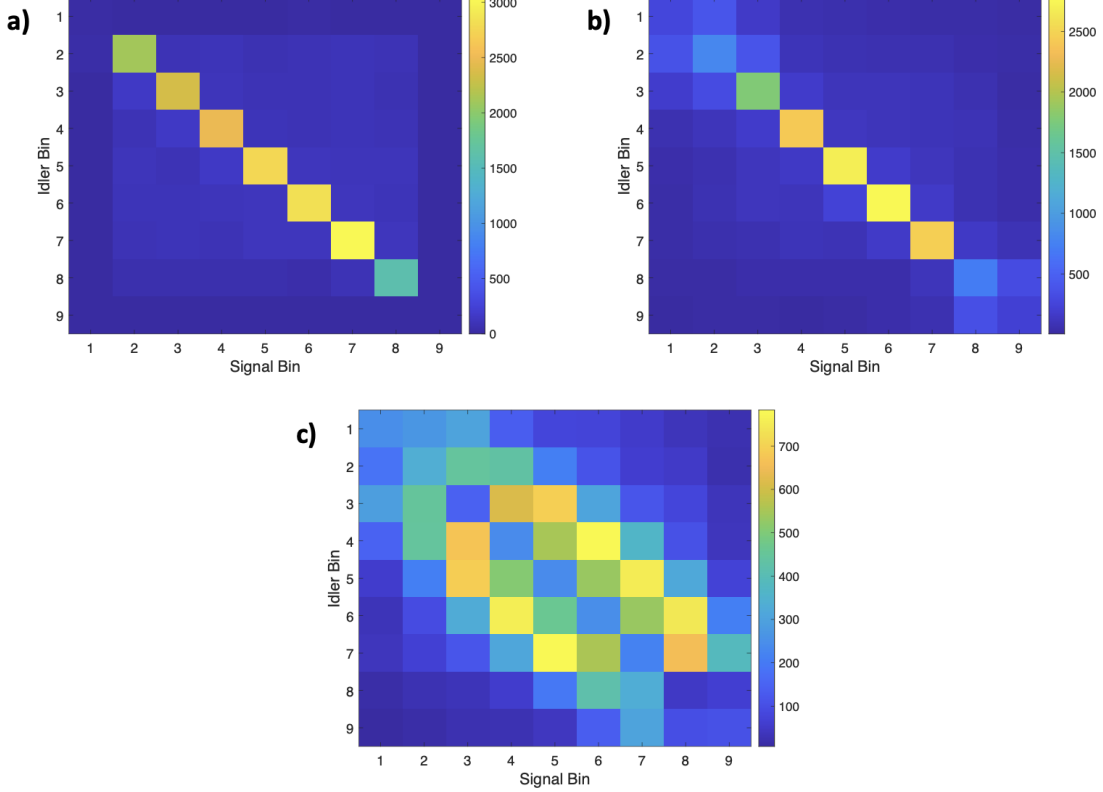


Figure 3.2. JSI data with: **a)** No RF signal **b)** RF modulation cancelled by destructive interference **c)** RF modulation interfering constructively. The acquisition time was 2 seconds per bin. For **a** and **b** the CAR ≈ 25

index of $\delta = 1.42$ radians. The experimental plot agrees very well with the simulated one. This experiment succeeded in obtaining truly nonlocal modulation cancellation. And the agreement between experiment and simulation when the modulators are driven in phase further validates the results. But the main purpose of this experiment was to show that the RFOF system can be used to synchronize QFPs at distant nodes in a quantum network. In this regard, this experiment was also successful. The RF signals driving the PMs remained stable enough to allow deterministic manipulation and detection of qubits.

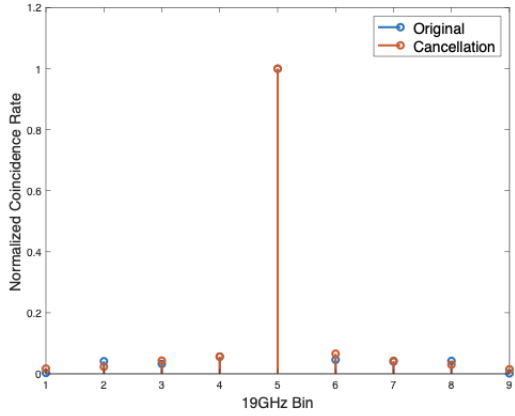


Figure 3.3. The 5th row of **Fig. 3.2 a** and **b** plotted. Cancelled sidebands are similar in magnitude to the original, ideal values.

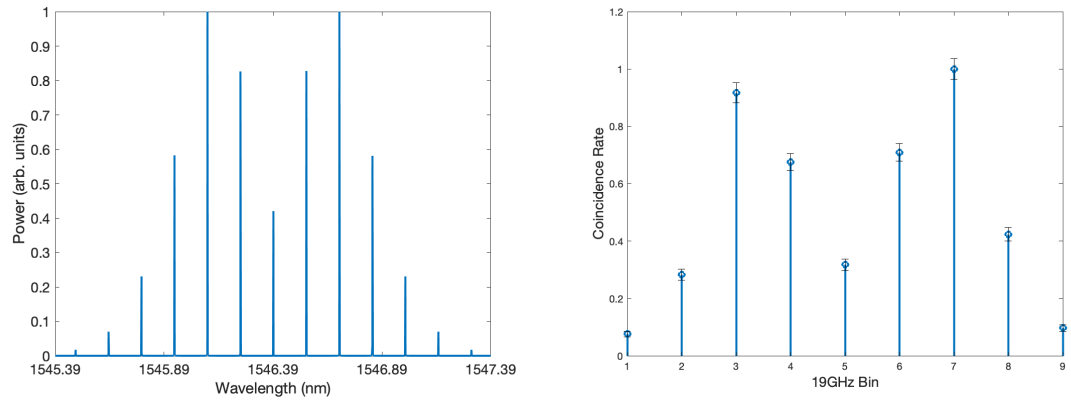


Figure 3.4. Left: Simulated sidebands for two PMs in series driven in phase. **Right:** The 5th row of **Fig. 3.2 c**, where the two PMs were driven in phase.

4. Conclusion and Future Work

This thesis presented the two phase modulator identity gate as a method to asses the drift between synchronized RF signals. This idea was first used to examine the quality of Agilent's built in 10 MHz synchronization system, and it was found that this system was inadequate. Instead, an RF over fiber system was constructed based on IMDD. When correctly setup and bias controlled, this system kept the identity gate stable for over an hour. This was tested over distances of up to 5km, and the RF signal drift remained less than 1 ps over a 30 min. trial.

Chapter 3 discusses testing this RFOF system in the quantum regime. Two PMs separated by 200 m represent two nodes in a quantum network. With a signal photon going through PM1 and an idler photon going through PM2, the system was able to cancel the modulation nonlocally. Additionally, the contrast between the in-phase and π out of phase results is stark, and even these preliminary results could be used for communication.

The immediate next step of this research is to do a direct comparison between the RFOF system and a White Rabbit module. The RFOF system has provided great stability, and a direct comparison test will definitively show how superior it is. In the near future, the RFOF synchronization will hopefully be used on distant QFPs for quantum communication demonstrations at ORNL. That was the original objective of this research, and the work covered in this thesis shows that we are well on our way to accomplishing it.

REFERENCES

- [1] L. Mandel and E. Wolf, *Optical Coherence and Quantum Optics*. Cambridge: Cambridge University Press, 1995.
- [2] J. S. Bell, “On the einstein podolsky rosen paradox,” *Physics Physique Fizika*, vol. 1, pp. 195–200, 3 Nov. 1964. DOI: [10.1103/PhysicsPhysiqueFizika.1.195](https://doi.org/10.1103/PhysicsPhysiqueFizika.1.195). [Online]. Available: <https://link.aps.org/doi/10.1103/PhysicsPhysiqueFizika.1.195>.
- [3] J. F. Clauser, M. A. Horne, A. Shimony, and R. A. Holt, “Proposed experiment to test local hidden-variable theories,” *Phys. Rev. Lett.*, vol. 23, pp. 880–884, 15 Oct. 1969. DOI: [10.1103/PhysRevLett.23.880](https://doi.org/10.1103/PhysRevLett.23.880). [Online]. Available: <https://link.aps.org/doi/10.1103/PhysRevLett.23.880>.
- [4] B. e. a. Hensen, “Loophole-free bell inequality violation using electron spins separated by 1.3 kilometers.,” *Nature*, vol. 526, pp. 682–686, 2015. [Online]. Available: <https://doi.org/10.1038/nature15759>.
- [5] S. Ramelow, L. Ratschbacher, A. Fedrizzi, N. K. Langford, and A. Zeilinger, “Discrete tunable color entanglement,” *Phys. Rev. Lett.*, vol. 103, p. 253601, 25 Dec. 2009. DOI: [10.1103/PhysRevLett.103.253601](https://doi.org/10.1103/PhysRevLett.103.253601). [Online]. Available: <https://link.aps.org/doi/10.1103/PhysRevLett.103.253601>.
- [6] L. Olislager, J. Cussey, A. T. Nguyen, *et al.*, “Frequency-bin entangled photons,” *Phys. Rev. A*, vol. 82, p. 013804, 1 Jul. 2010. DOI: [10.1103/PhysRevA.82.013804](https://doi.org/10.1103/PhysRevA.82.013804). [Online]. Available: <https://link.aps.org/doi/10.1103/PhysRevA.82.013804>.
- [7] J. A. Jaramillo-Villegas, P. Imany, O. D. Odele, *et al.*, “Persistent energy–time entanglement covering multiple resonances of an on-chip biphoton frequency comb,” *Optica*, vol. 4, no. 6, pp. 655–658, Jun. 2017. DOI: [10.1364/OPTICA.4.000655](https://doi.org/10.1364/OPTICA.4.000655). [Online]. Available: <https://opg.optica.org/optica/abstract.cfm?URI=optica-4-6-655>.
- [8] e. a. Kues M., “Quantum optical microcombs,” *Nature Photonics*, 2019.
- [9] H.-H. Lu, “Quantum information processing with frequency-bin qudits,” Ph.D. dissertation, Purdue University, 2020.

- [10] P. Imany, O. D. Odele, J. A. Jaramillo-Villegas, D. E. Leaird, and A. M. Weiner, “Characterization of coherent quantum frequency combs using electro-optic phase modulation,” *Phys. Rev. A*, vol. 97, p. 013813, 1 Jan. 2018. doi: [10.1103/PhysRevA.97.013813](https://doi.org/10.1103/PhysRevA.97.013813). [Online]. Available: <https://link.aps.org/doi/10.1103/PhysRevA.97.013813>.
- [11] J. Lukens, “Novel applications of photonic signal processing: Temporal cloaking and biphoton pulse shaping,” Ph.D. dissertation, Purdue University, 2015.
- [12] H. Haus, *Waves and Fields in Optoelectronics*. New Jersey: Prentice-Hall, Inc., 1984.
- [13] R. Boyd, *Nonlinear Optics*. London: Elsevier Inc., 2020.
- [14] V. e. a. Urick, *Fundamentals of Microwave Photonics*. New Jersey: Wiley Sons Inc, 2015.
- [15] O. Sandoval, “Electro-optic phase modulation, frequency comb generation, nonlinear spectral broadening, and applications,” Ph.D. dissertation, Purdue University, 2019.
- [16] W. Arfken and Harris., *Mathematical Methods for Physicists*. Waltham: Elsevier Inc, 2013.
- [17] D. P. DiVincenzo, “The physical implementation of quantum computation,” *Fortschritte der Physik*, vol. 48, no. 9-11, pp. 771–783, 2000. doi: [https://doi.org/10.1002/1521-3978\(200009\)48:9/11<771::AID-PROP771>3.0.CO;2-E](https://doi.org/10.1002/1521-3978(200009)48:9/11<771::AID-PROP771>3.0.CO;2-E). eprint: <https://onlinelibrary.wiley.com/doi/pdf/10.1002/1521-3978%28200009%2948%3A9/11%3C771%3A%3AAID-PROP771%3E3.0.CO%3B2-E>. [Online]. Available: <https://onlinelibrary.wiley.com/doi/abs/10.1002/1521-3978%28200009%2948%3A9/11%3C771%3A%3AAID-PROP771%3E3.0.CO%3B2-E>.
- [18] e. a. Alshowkan Muneer, “A reconfigurable quantum local area network over deployed fiber,” *PRX Quantum*, 2021.
- [19] A. M. Weiner, *Ultrafast Optics*. New Jersey: John Wiley Sons Inc., 2009.
- [20] H.-H. Lu, M. Liscidini, A. L. Gaeta, A. M. Weiner, and J. M. Lukens, “Frequency-bin photonic quantum information,” *Optica*, vol. 10, no. 12, p. 1655, Dec. 2023, ISSN: 2334-2536. doi: [10.1364/optica.506096](https://doi.org/10.1364/optica.506096). [Online]. Available: <http://dx.doi.org/10.1364/OPTICA.506096>.

- [21] S. E. Harris, “Nonlocal modulation of entangled photons,” *Phys. Rev. A*, vol. 78, p. 021807, 2 Aug. 2008. doi: [10.1103/PhysRevA.78.021807](https://doi.org/10.1103/PhysRevA.78.021807). [Online]. Available: <https://link.aps.org/doi/10.1103/PhysRevA.78.021807>.
- [22] S. Sensarn, G. Y. Yin, and S. E. Harris, “Observation of nonlocal modulation with entangled photons,” *Phys. Rev. Lett.*, vol. 103, p. 163601, 16 Oct. 2009. doi: [10.1103/PhysRevLett.103.163601](https://doi.org/10.1103/PhysRevLett.103.163601). [Online]. Available: <https://link.aps.org/doi/10.1103/PhysRevLett.103.163601>.
- [23] J. D. Franson, “Nonlocal cancellation of dispersion,” *Phys. Rev. A*, vol. 45, no. 5, pp. 3126–3132, Mar. 1992, ISSN: 1094-1622. doi: [10.1103/physreva.45.3126](https://doi.org/10.1103/physreva.45.3126). [Online]. Available: <http://dx.doi.org/10.1103/PhysRevA.45.3126>.
- [24] S.-Y. Baek, Y.-W. Cho, and Y.-H. Kim, “Nonlocal dispersion cancellation using entangled photons,” *Opt. Express*, vol. 17, no. 21, pp. 19 241–19 252, Oct. 2009. doi: [10.1364/OE.17.019241](https://doi.org/10.1364/OE.17.019241). [Online]. Available: <http://www.opticsexpress.org/abstract.cfm?URI=oe-17-21-19241>.
- [25] K. A. O’Donnell, “Observations of dispersion cancellation of entangled photon pairs,” *Phys. Rev. Lett.*, vol. 106, p. 063601, 6 Feb. 2011. doi: [10.1103/PhysRevLett.106.063601](https://doi.org/10.1103/PhysRevLett.106.063601). [Online]. Available: <https://link.aps.org/doi/10.1103/PhysRevLett.106.063601>.
- [26] J. M. Lukens, A. Dezfooliyan, C. Langrock, M. M. Fejer, D. E. Leaird, and A. M. Weiner, “Demonstration of high-order dispersion cancellation with an ultrahigh-efficiency sum-frequency correlator,” *Phys. Rev. Lett.*, vol. 111, p. 193603, 19 2013.
- [27] M. Bloch, S. W. McLaughlin, J.-M. Merolla, and F. Patois, “Frequency-coded quantum key distribution,” *Opt. Lett.*, vol. 32, no. 3, pp. 301–303, Feb. 2007. doi: [10.1364/OL.32.000301](https://doi.org/10.1364/OL.32.000301). [Online]. Available: <http://ol.osa.org/abstract.cfm?URI=ol-32-3-301>.
- [28] L. Olislager, J. Cussey, A. T. Nguyen, *et al.*, “Frequency-bin entangled photons,” *Phys. Rev. A*, vol. 82, p. 013804, 1 Jul. 2010. doi: [10.1103/PhysRevA.82.013804](https://doi.org/10.1103/PhysRevA.82.013804). [Online]. Available: <https://link.aps.org/doi/10.1103/PhysRevA.82.013804>.
- [29] S. Seshadri, N. Lingaraju, H.-H. Lu, P. Imany, D. E. Leaird, and A. M. Weiner, “Nonlocal subpicosecond delay metrology using spectral quantum interference,” *Optica*, vol. 9, no. 12, pp. 1339–1346, 2022.

- [30] H.-H. Lu, N. A. Peters, A. M. Weiner, and J. M. Lukens, “Characterization of quantum frequency processors,” *IEEE J. Sel. Top. Quantum Electron.*, vol. 29, no. 6, p. 6 300 112, 2023. DOI: [10.1109/JSTQE.2023.3266662](https://doi.org/10.1109/JSTQE.2023.3266662).
- [31] H.-H. Lu, M. Alshowkan, K. V. Myilswamy, A. M. Weiner, J. M. Lukens, and N. A. Peters, “Generation and characterization of ultrabroadband polarization–frequency hyperentangled photons,” *Opt. Lett.*, vol. 48, no. 22, pp. 6031–6034, Nov. 2023. DOI: [10.1364/OL.503127](https://doi.org/10.1364/OL.503127). [Online]. Available: <https://opg.optica.org/ol/abstract.cfm?URI=ol-48-22-6031>.
- [32] M. Lipiski, T. Wostowski, J. Serrano, and P. Alvarez, “White Rabbit: A PTP application for robust sub-nanosecond synchronization,” in *IEEE Int. Sym. Precision Clock Sync. Meas. Contr. Commun.*, 2011, pp. 25–30. DOI: [10.1109/ISPCS.2011.6070148](https://doi.org/10.1109/ISPCS.2011.6070148). [Online]. Available: <https://doi.org/10.1109/ispcs.2011.6070148>.
- [33] M. Rizzi, M. Lipinski, P. Ferrari, S. Rinaldi, and A. Flammini, “White Rabbit clock synchronization: Ultimate limits on close-in phase noise and short-term stability due to FPGA implementation,” *IEEE Trans. Ultrason. Ferroelectr. Freq. Control.*, vol. 65, pp. 1726–1737, 2018. DOI: [10.1109/TUFFC.2018.2851842](https://doi.org/10.1109/TUFFC.2018.2851842).
- [34] S. M. Foreman, K. W. Holman, D. D. Hudson, D. J. Jones, and J. Ye, “Remote transfer of ultrastable frequency references via fiber networks,” *Rev. Sci. Instrum.*, vol. 78, no. 2, p. 021 101, 2007. DOI: [10.1063/1.2437069](https://doi.org/10.1063/1.2437069).
- [35] . liwczyski, P. Krehlik, and M. Lipiski, “Optical fibers in time and frequency transfer,” *Meas. Sci. Technol.*, vol. 21, no. 7, p. 075 302, 2010. DOI: [10.1088/0957-0233/21/7/075302](https://doi.org/10.1088/0957-0233/21/7/075302).